PAPER

Nanoconfinement of ultra-small Bi$_2$Te$_3$ nanocrystals on reduced graphene oxide: a pathway to high-performance sodium-ion battery anodes†

Zhuoying Cheng, Zhuo Li, Yuao Wang, Yiyang Mao, Jun Yan,* Dianxue Cao [ID] and Kai Zhu [ID] *

Bismuth telluride (Bi$_2$Te$_3$) nanomaterials have attracted considerable attention owing to their intriguing physicochemical properties and wide-ranging potential applications arising from their distinctive layered structure and nanoscale size effects. However, synthesizing sub-100 nm ultra-small Bi$_2$Te$_3$ nanocrystals remains a formidable challenge. To date, there has been little investigation on the performance of these ultra-small Bi$_2$Te$_3$ nanocrystals in sodium-ion batteries (SIBs). This study presents a general strategy for synthesizing ultra-small Bi$_2$Te$_3$ nanocrystals on reduced graphene oxide (Bi$_2$Te$_3$/rGO) through a nanoconfinement approach. First-principles calculations and electrochemical kinetic studies confirm that the ultra-small Bi$_2$Te$_3$/rGO composite material can effectively mitigate volumetric expansion, preserve electrode integrity, and enhance electron transfer, Na-ion adsorption, and diffusion capacity. As a result, the Bi$_2$Te$_3$/rGO electrode demonstrates a remarkable initial specific capacity of 521 mA h g^{-1} at 0.1 A g^{-1}, showcasing outstanding rate behaviour and long-lasting cycle life exceeding 800 cycles at 1 A g^{-1} while preserving exceptional rate properties. The function of the battery is indicated by *ex situ* TEM and XPS findings, which propose a conventional dual mechanism involving conversion and alloying. This work paves the way for rapid advancements in Bi$_2$Te$_3$-based SIB anodes while contributing to our understanding of sodium ion storage mechanisms.

1. Introduction

The abundant availability of sodium in nature, its low cost, and the rocking-chair Na-ion storage mechanism have led to significant research interest in sodium-ion batteries (SIBs) as a potential alternative to lithium-ion batteries, as evidenced by the attention they have received.[1,2] On the other hand, the Na ion demonstrates reduced reaction kinetics and transport during electrochemical cycling because of its greater ionic radius (around 1.02 Å). It is accompanied by a notable increase in volume, which dramatically affects the electrode's structural stability while charging and discharging.[3,4] Consequently, the primary challenge faced by exploring suitable SIB anode materials lies in achieving excellent structural stability while accommodating volume changes induced by Na ion transport and providing rapid Na ion transport capabilities.[5,6]

In recent years, there has been significant emphasis on the development of efficient anode substances to increase the capacity of sodium-ion batteries.[7,8] Due to their high theoretical conversion capacity, sulfides, selenides, and metal oxides have gained considerable attention among alternative materials.[9,10] Compared with sulfides and oxides, metal tellurides (MTs) exhibit enhanced electrical conductivity and electrochemical activity,[9,11] making them promising candidates as anode materials for SIBs. However, further improvements in their rate capability are still necessary to meet practical demands.[12,13] Among various MT materials, Bi$_2$Te$_3$ possesses a layered structure similar to graphite and demonstrates adequate theoretical capacity through a combination of conversion and alloying reactions.[14,15] Nevertheless, the main obstacle related to Bi$_2$Te$_3$ is its significant alteration in volume while cycling, resulting in the pulverization of the electrode substance and a rapid decline in capacity.[16,17] Enhancing the rate capability of MTs while addressing the volume change of Bi$_2$Te$_3$ represents a crucial objective toward advancing SIB anode materials.[18]

Researchers have developed alternative methods for fabricating Bi$_2$Te$_3$-based nanocomposites to enhance the performance of SIBs that overcome the limitations of conventional

electrode preparation methods. One frequently used method includes combining Bi_2Te_3 with a conductive carbon framework to create nanocomposites, which enhances the stability of the active material's structure and improves its electrical conductivity.[19] Several remarkable studies have demonstrated that including nanoscale substances can notably enhance the surface area of contact between the electrode and electrolyte, enlarge ion storage locations, and reduce the length of ion transport routes. These enhancements contribute to the improvement in reversible capacity and kinetic performance.[20–22] Moreover, the high electronic conductivity of carbon facilitates accelerated electron transfer, further enhancing the rate capability. For instance, Chong *et al.* synthesized a composite anode architecture of Bi_2Te_3 nanosheets enclosed within reduced graphene oxide (rGO) and nitrogen-doped carbon (NC) layers. At a rate of 0.05 A g^{-1}, the composite displayed an impressive initial reversible specific capacity of 322.7 mA h g^{-1} while also demonstrating outstanding stability throughout multiple cycles and excellent performance at different rates.[23] Pang *et al.* fabricated solvent-reduced Bi_2Te_3 nanosheets with exceptional rate capability and long-term cycling performance by delivering 364.0 mA h g^{-1} after 1200 cycles at 5 A g^{-1}.[24]

This work describes the fabrication of ultra-small Bi_2Te_3 nanocrystals uniformly attached to reduced graphene oxide (rGO) nanosheets using a facile and versatile nanoconfinement strategy. The pH adjustment of the dispersion of graphene oxide leads to a slight stacking of graphene oxide sheets as a result of reduced electrostatic repulsion. *In situ* growth of ultra-small Bi_2Te_3 nanocrystals in these weakly stacked graphene oxide sheets was achieved using confined nano-reactors. By taking advantage of its tiny size, the Bi_2Te_3/rGO composite material, consisting of just one sheet, is utilized as an anode material for SIBs, exhibiting an impressive maximum capacity of 521 mA h g^{-1} at 0.1 A g^{-1} coupled with exceptional rate performance and remarkable cycling stability. The storage mechanism of sodium ions in Bi_2Te_3/rGO was elucidated through *ex situ* transmission electron microscopy (TEM) and *ex situ* X-ray photoelectron spectroscopy (XPS). In addition, successfully assembling a high-performing full cell further displays the potential application of MT anodes for SIBs.

2. Results and discussion

The diagram of synthesizing Bi_2Te_3 nanocrystals on rGO is depicted in Fig. 1A. First, dilute nitric acid was dropped into a homogeneous dispersion of GO until the pH reaches approximately 4, resulting in a slight accumulation of GO nanosheets. Subsequently, $Bi(NO_3)_3 \cdot 5H_2O$ was added to the mixture while stirring it in an ice bath to regulate the nucleation and growth speed of the GO dispersion. Through coordination/electrostatic interactions with oxygen-containing functional groups, Bi^{3+} cations can adsorb on the surface of GO. Then, NH_4Cl was added to the dispersion to inhibit the expansion of extremely tiny BiOCl nanocrystals in the interlayer nano region between

the loosely arranged GO nanosheets. After subjecting to centrifugal purification and freeze drying, the end product was transformed into a composite aerogel. Utilizing BiOCl/GO nanosheets as precursors and Na_2TeO_3 as a tellurizing agent, Bi_2Te_3/GO was obtained through an ion exchange process under hydrothermal conditions. Finally, by subjecting it to a simple annealing treatment at 350 °C, graphene oxide was effectively reduced, leading to the successful synthesis of chemically bonded ultra-small Bi_2Te_3 on reduced graphene oxide (referred to as Bi_2Te_3/rGO).

The scanning electron microscopy (SEM) images in Fig. 1A and S1† illustrate the even dispersion of Bi_2Te_3 nanoparticles throughout the rGO surface. The images reveal a close contact between Bi_2Te_3 nanoparticles and rGO, with loosely arranged GO nanosheets offering numerous locations for the formation of tiny Bi_2Te_3 nanocrystals and an important interlayer confinement nano-space. For comparison, Bi_2Te_3 nanoparticles of a larger size (approximately 550 nm on average) were produced by a commonly employed solvothermal method (Fig. S2, ESI†). Weakly stacked GO nanosheets aid in nucleation for ultra-small Bi_2Te_3 nanocrystals, playing a significant role in interlayer confinement. The microstructure of Bi_2Te_3–rGO (Fig. 1C–G) was examined using transmission electron microscopy (TEM) analysis, which showed a homogeneous dispersion of tiny Bi_2Te_3 nanoparticles on the rGO surface with no evidence of clustering. As shown in the high-resolution TEM image (Fig. 1F), a lattice spacing corresponding to the (002) plane of Bi_2Te_3 at 0.37 nm is observed. Fig. 1G displays the selected area electron diffraction (SAED) pattern that reveals diffraction spots corresponding to the (015), (110), and (125) planes of Bi_2Te_3. Dark-field TEM imaging and energy-dispersive spectroscopy elemental mapping confirm the presence of elements including Bi, Te, C, and O on both the rGO flakes and ultra-small Bi_2Te_3 nanoparticles.

Fig. 2A illustrates the XRD pattern of Bi_2Te_3/rGO, displaying clear peaks at $2\theta = 8.6°$, $17.4°$, $23.6°$, $27.6°$, $37.8°$, $40.4°$, $41.1°$, and $50.1°$, which correspond to the (003), (006), (101), (015), (1010), (0111), (110), and (205) crystallographic planes of Bi_2Te_3, respectively. These peaks align excellently with the standard card reference JCPDS no. 04-004-7783, confirming the successful synthesis of Bi_2Te_3/rGO by the ion exchange method. Fig. S3† shows the XRD pattern of BiOCl. Raman spectroscopy, depicted in Fig. 2B, was employed to investigate the carbon state within the composite material. The wavenumbers at around 1589 and 1341 cm^{-1} are attributed to the sp^2-hybridized carbon (g-band) and sp^3-hybridized carbon (d-band) in Bi_2Te_3/rGO.[16,25,26] In addition, the rGO content was determined using thermogravimetric analysis (TG). After heating Bi_2Te_3 to 800 °C in air, it completely transforms into TeO_2 and Bi_2O_3. The TG curve (Fig. 2C) reveals that the rGO content in Bi_2Te_3/rGO is approximately 3.8 wt%. According to Table S1 in the ESI,† the electrical conductivity of Bi_2Te_3 nanoparticles is 0.33×10^{-2} S cm^{-1}, while that for Bi_2Te_3/rGO composites is 1.47×10^{-2} S cm^{-1}, indicating that rGO contributes to the enhancement of electrical conductivity in Bi_2Te_3/rGO. The N_2 adsorption/desorption isotherms of Bi_2Te_3 and Bi_2Te_3/
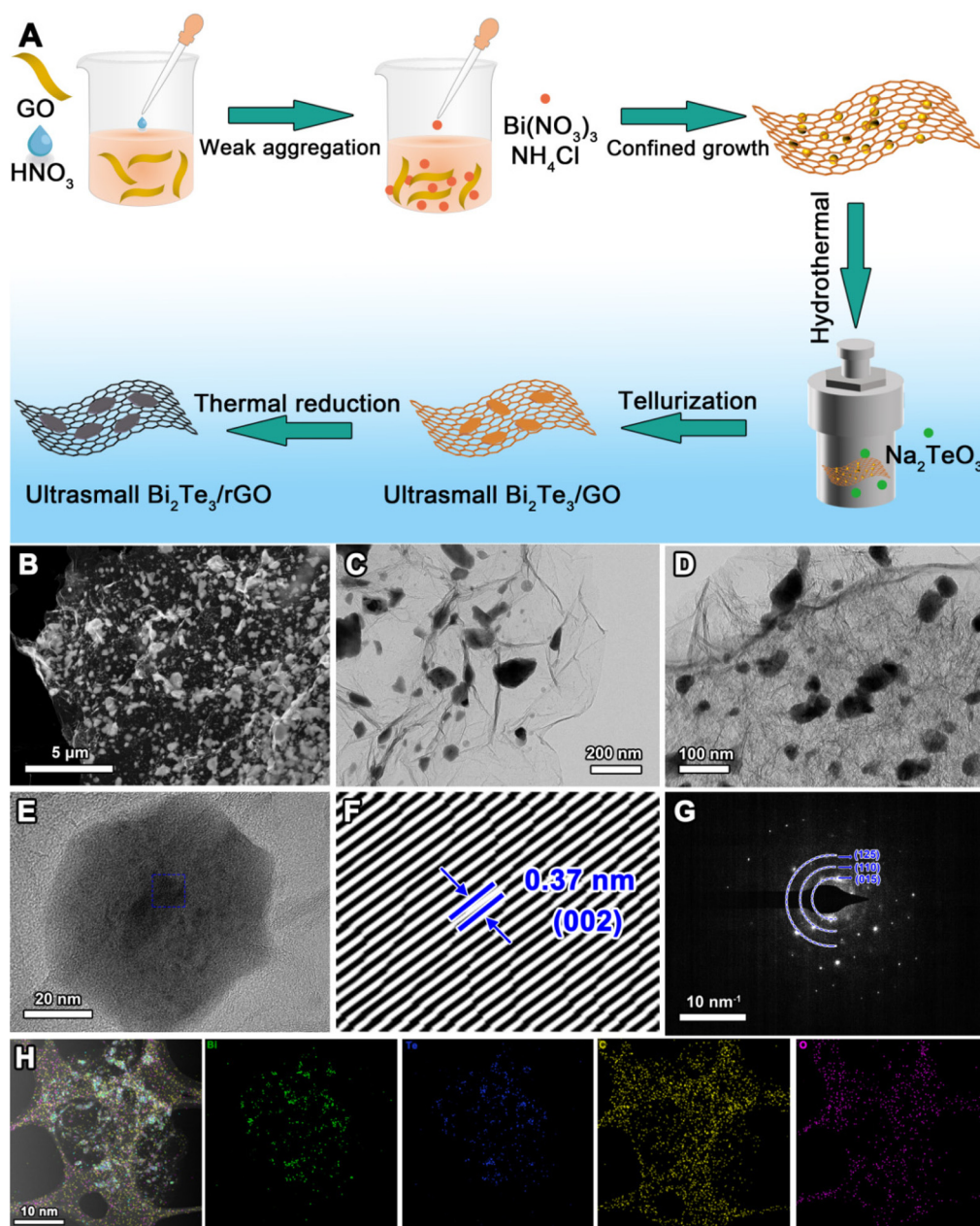
Fig. 1 (A) Illustration of the materials synthesis process; (B) SEM image of Bi_2Te_3/rGO, (C and D) TEM images of Bi_2Te_3/rGO; (F) HRTEM image of Bi_2Te_3/rGO, (G) SAED pattern of Bi_2Te_3/rGO; (H) EDS mapping image of Bi_2Te_3/rGO.

rGO (Fig. 2D) display characteristic hysteresis loops,[27] indicative of a type-IV mesoporous structure in both composite materials, with the pore sizes of these composites vary from 2 nm to 100 nm. The BET specific surface area of Bi_2Te_3 was found to be 3.79 m^2 g^{-1}, while that of Bi_2Te_3/rGO significantly increases to approximately 24.21 m^2 g^{-1}. This suggests that adding rGO affected the original multichannel structure of Bi_2Te_3/rGO. The BET findings suggest that Bi_2Te_3/rGO possesses a significantly increased specific surface area, indicating potential advantages in facilitating electrolyte permeation and providing a greater abundance of active sites for Na ion electrochemical interactions.

The X-ray photoelectron spectroscopy (XPS) technique was employed to investigate the composition and valence states of Bi_2Te_3/rGO. In the exhaustive scan XPS measurement profile, Bi, Te, C, and O elemental components were observed in the Bi_2Te_3/rGO sample (Fig. 2E). The C 1s core level spectra exhibited five well-fitted peaks at 288.5, 287.6, 286.2, 285.3, and 284.6 eV, corresponding to the O–C=O, C–Te, C–O, C=O, and C–C bonds, respectively.[9,28] Fig. 2G shows the O 1s spectra of Bi_2Te_3/rGO, where the three fitted peaks at 533.1, 531.3, and 530.2 eV are attributed to the C–O–C, Bi–O–C, and Bi–O bonds, respectively.[29,30] It is worth noting that the Bi–O–C chemical bond between rGO and Bi_2Te_3 facilitates rapid charge transfer while
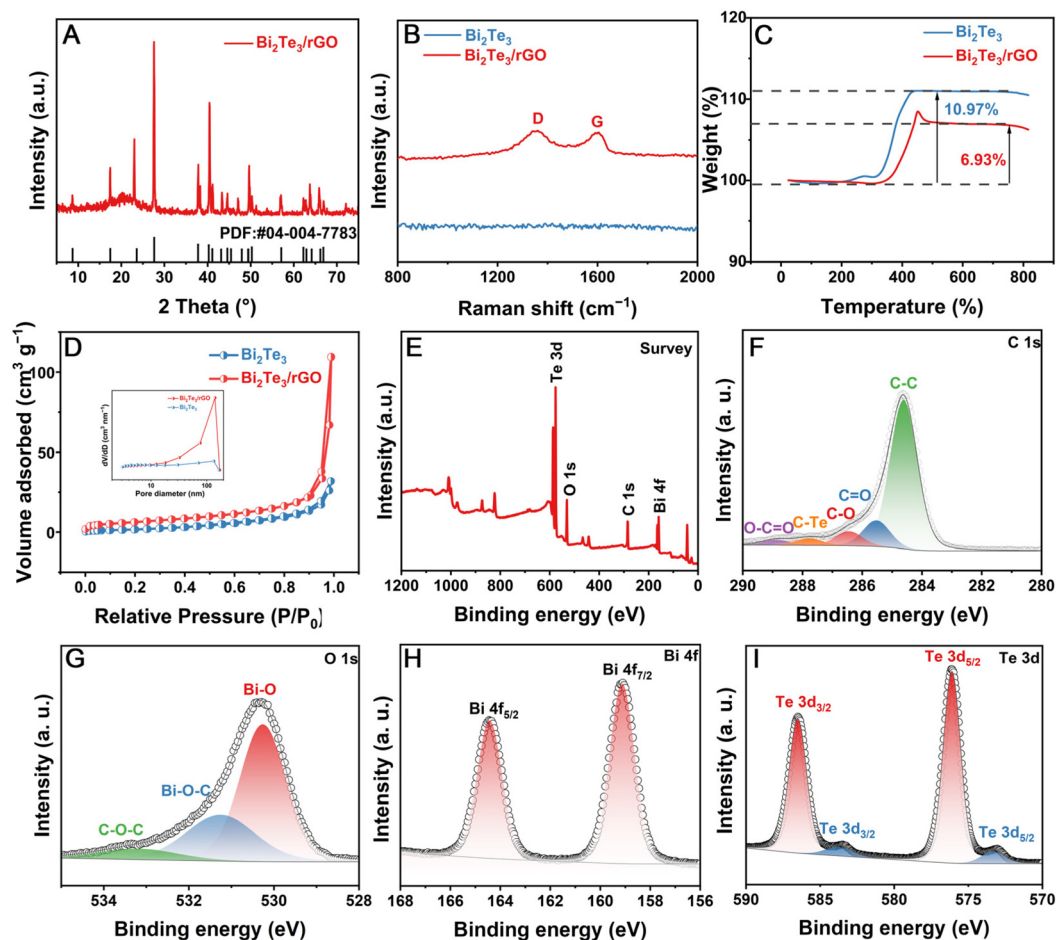
Fig. 2 (A) XRD pattern of Bi$_2$Te$_3$/rGO; (B) Raman spectra, (C) thermogravimetric analysis, and (D) nitrogen adsorption–desorption isotherms and pore size distribution curves of Bi$_2$Te$_3$/rGO; XPS spectra of Bi$_2$Te$_3$/rGO: (E) full spectrum, (F) C 1s, (G) O 1s (H) Bi 4f and (I) Te 3d.

maintaining good morphological and structural stability. The 4f$_{5/2}$ and Bi 4f$_{7/2}$ inherent peaks (Fig. 2H) are represented by the two separate peaks at 164.5 eV and 159.5 eV, respectively.[28] The binding energy peaks observed at 586.4 eV and 576.1 eV are attributed to the presence of the Te–O bond, indicating the surface oxidation of Te atoms.[31] In Fig. 2I, the XPS spectrum of Te 3d shows the presence of two distinct pairs of peaks. The Te 3d$_{3/2}$ and Te 3d$_{5/2}$ states linked to the Bi–Te bond in the Bi$_2$Te$_3$ compound can be identified as the peaks at 583.6 eV and 573.2 eV.[32]

To elucidate the intrinsic advantages and the sodium ion storage mechanism of Bi$_2$Te$_3$, a half-cell system was employed with metal sodium as the counter electrode, using the corresponding electrochemical testing methods. During the first cathodic scan of the cyclic voltammetry(CV) curves, the Bi$_2$Te$_3$ cathodic peaks (Fig. 3A) were detected at 1.1 V, suggesting the development of a solid electrolyte interface (SEI) and the presence of specific unfavorable reactions.[33,34] The conversion reaction from Bi$_2$Te$_3$ to Bi (eqn (1)) can be identified as the cause of the cathodic peak appearing at 1.5 V.[35,36] The alloy reactions of Bi (eqn (2) and (3)) are represented by the two peaks at 0.4 V and 0.6 V.[37] The peak at 0.2 V may be attributed to carbon materials.[38] As oxidation occurs, the cliffs at 0.6 V

and 0.8 V correspond to the gradual dissociation of the Na$_3$Bi alloy into Bi (eqn (4) and (5)). Furthermore, the oxidation peak at 1.9 V appears as a result of the dissociation reaction of Na$_2$Te (eqn (6)). The CV curves of the Bi$_2$Te$_3$/rGO anode remain highly consistent in the subsequent three cycles, demonstrating the exceptional reversibility of the phase transition throughout the cycling process. Therefore, the entire electrochemical reactions involved in the Bi$_2$Te$_3$/rGO anode for SIBs can be described by the following equations:[38]

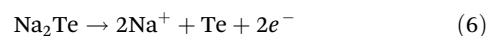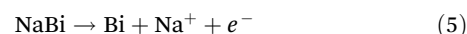$$Bi_2Te_3 + 6Na^+ + 6e^- \rightarrow 3Na_2Te + 2Bi \quad (1)$$

$$Bi + Na^+ + e^- \rightarrow NaBi \quad (2)$$

$$NaBi + 2Na^+ + 2e^- \rightarrow Na_3Bi \quad (3)$$

$$Na_3Bi \rightarrow NaBi + 2Na^+ + 2e^- \quad (4)$$

$$NaBi \rightarrow Bi + Na^+ + e^- \quad (5)$$
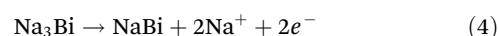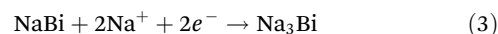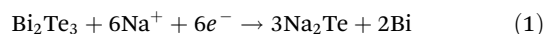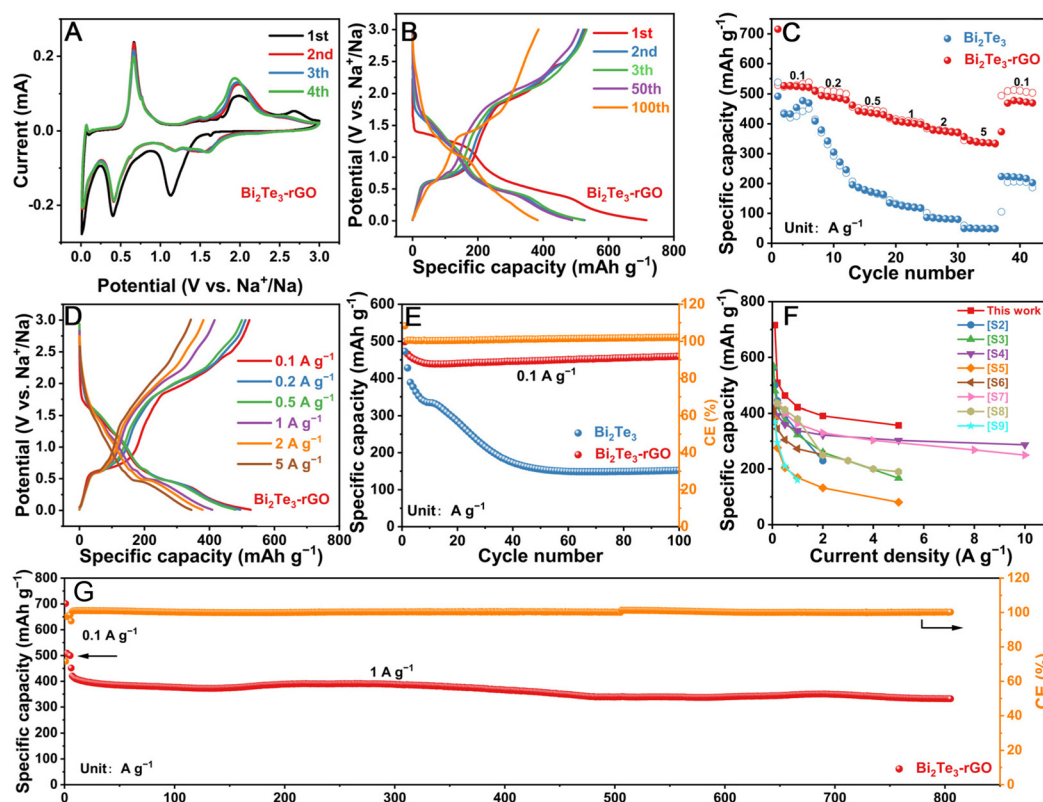
$$Na_2Te \rightarrow 2Na^+ + Te + 2e^- \quad (6)$$

Fig. 3B depicts the galvanostatic charge–discharge (GCD) curve at 0.1 A g^{-1}. Notably, two distinct discharge voltage

**Fig. 3** (A) CV profiles of Bi$_2$Te$_3$/rGO, (B) GCD curves of Bi$_2$Te$_3$/rGO, (C) rate capabilities of Bi$_2$Te$_3$ and Bi$_2$Te$_3$/rGO. (D) GCD curves of Bi$_2$Te$_3$/rGO, (E) rate performance comparison of Bi$_2$Te$_3$/rGO with other reported metal telluride for SIBs, (F) cycling performances of Bi$_2$Te$_3$ and Bi$_2$Te$_3$/rGO, (G) long-term cycling performance of Bi$_2$Te$_3$/rGO.

plateaus are observed at approximately 1.6 V and 0.4 V (*vs.* Na$^+$/Na), which aligns well with the CV curve. At a current density of 0.1 A g^{-1}, the Bi$_2$Te$_3$/rGO composite material demonstrates a remarkable initial coulombic efficiency (ICE) of 75.2%, with an initial discharge capacity of 719 mA h g^{-1} and a charge specific capacity of 539 mA h g^{-1}. After undergoing 100 cycles, the discharge capacity remains at 446 mA h g^{-1} with a cycle efficiency of 91.1%. In contrast, the discharge capacity of the pure Bi$_2$Te$_3$ electrode is close to 450 mA h g^{-1} at 0.1 A g^{-1} but significantly decreases to only 50 mA h g^{-1} at a current density of 5 A g^{-1}. Upon restoring the current density to 0.1 A g^{-1}, the specific capacity only reaches 222 mA h g^{-1}. In sharp contrast, the Bi$_2$Te$_3$/rGO composite material exhibits discharge capacities of 521, 488, 436, 433, and 374 mA h g^{-1} at 0.1, 0.2, 0.5, 1, and 2 A g^{-1}, respectively. Even at 5 A g^{-1}, it maintains a remarkable specific capacity of 340 mA h g^{-1}. In addition, upon restoring the current to 0.1 A g^{-1}, the Bi$_2$Te$_3$/rGO composite material exhibits a sustained higher specific degree of 476 mA h g^{-1}, demonstrating its superior rate capability compared to pure Bi$_2$Te$_3$ (Fig. 3C). The improved rate efficiency of the Bi$_2$Te$_3$/rGO composite material can be ascribed to the combined impact of the ultra-small Bi$_2$Te$_3$ nanocrystal arrangement and the enhanced chemical bonding between Bi$_2$Te$_3$ and conductive rGO.

Fig. 3D depicts the GCD patterns of Bi$_2$Te$_3$/rGO electrodes at different current densities in the range of 0.1–5 A g^{-1}. The

cycling performance was evaluated at a high current density of 1 A g^{-1}. Fig. 3E demonstrates that the specific capacity of the pure Bi$_2$Te$_3$ electrode experiences a sharp decline within the initial 40 cycles, whereas the Bi$_2$Te$_3$/rGO electrode maintains a relatively stable specific capacity of 499 mA h g^{-1} throughout the cycling process. Notably, the specific capacity and rate performance of the Bi$_2$Te$_3$/rGO composite material significantly surpass those of previously reported bismuth-based anode electrode materials (Fig. 3F, Table S2†). Before engaging in extended cycling at elevated current densities, a preliminary activation test was carried out at a reduced current density of 0.1 A g^{-1}, involving six charge–discharge cycles. During the first 100 cycles, the specific capacity experiences a decrease from 421 to 387 mA h g^{-1}. Remarkably, the system demonstrates exceptional stability with an impressive specific capacity of 345 mA h g^{-1} achieved after 800 consecutive cycles, resulting in a capacity retention rate of 82% (Fig. 3G). The outstanding performance observed in the anode electrode of Bi$_2$Te$_3$/rGO can be ascribed to its distinctive architectural configuration, wherein minuscule Bi$_2$Te$_3$ nanocrystals establish chemical connections on a three-dimensional interconnected graphene network, facilitating rapid ion and electron transfer across the entire electrode surface.

The capacitance contribution is a crucial parameter for assessing the high rate performance of electrode materials. The dynamic capacitance contribution of the Bi$_2$Te$_3$/rGO elec-
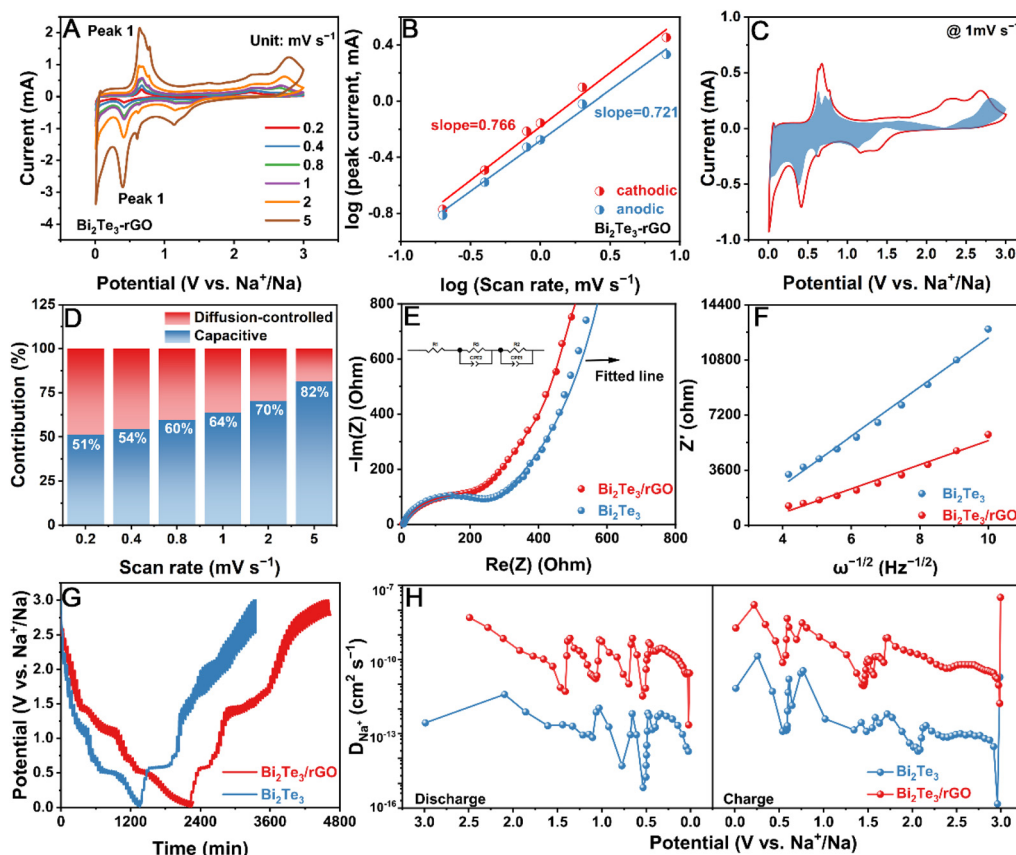
Fig. 4 (A) CV profiles of Bi_2Te_3/rGO at different scan rates ranging from 0.2 to 5 mV s^{-1}. (B) A linear relationship existing between the peak current logarithm and the scan rate logarithm. (C) Capacitive contribution of the Bi_2Te_3/rGO electrode at a scan rate of 1.0 mV s^{-1}. (D) Contributions from capacitive- and diffusion-controlled sources at different scan rates. (E) EIS spectra of Bi_2Te_3 and Bi_2Te_3/rGO, with an equivalent circuit model fitted to the data shown in the inset figure. (F) Correlation between Z' and $\omega^{-1/2}$ for the Bi_2Te_3 and Bi_2Te_3/rGO electrodes. (G) GITT values and (H) calculated diffusion coefficients (D_{Na^+}) of the Bi_2Te_3 and Bi_2Te_3/rGO electrodes.

trode was determined by plotting CV profiles at different scan rates (0.2–5 mV s^{-1}), as illustrated in Fig. 4A. The correlation between the peak current (i) and the scan rate (v) in the CV curves conforms to eqn (7), where adjustable parameters a and b are utilized:

$$i = av^b \tag{7}$$

The slope of log(i) relative to log(v) in the graph represents the value of b. The calculated values for b obtained from anodic peak 1 and cathodic peak 2 are 0.721 and 0.766, respectively (Fig. 4B), implying that the capacitance process contributes predominantly to the capacity. The contributions of ion diffusion and pseudocapacitive diffusion at different scan rates (v) can be derived from eqn (8):

$$i(v) = k_1v + k_2v^{1/2} \tag{8}$$

where k_1v represents the contribution of pseudocapacitive diffusion, while $k_2v^{1/2}$ represents the contribution of ion diffusion.[39,40] As depicted in Fig. 4C, the pseudo-capacitance contribution rate of Bi_2Te_3/rGO at 1 mV s^{-1} was determined to be 64% (blue region). Fig. 4D shows that the Bi_2Te_3/rGO elec-

trode has capacitance contribution rates of 51%, 54%, 60%, 64%, 70%, and 82% at scan rates of 0.2, 0.4, 0.8, 1, 2, and 5 mV s^{-1}, respectively. The gradual increase in capacitance contribution results in more favourable characteristics during rapid charge and discharge processes. The effective growth of unique Bi_2Te_3 nanoparticles on a three-dimensional rGO structure is primarily responsible for high capacitance control as it provides superior conductivity and abundant active sites for Na$^+$ accommodation.

To elucidate the enhanced electrochemical capabilities of Bi_2Te_3/rGO composite materials, electrochemical impedance spectroscopy (EIS) analysis was performed on both the pure Bi_2Te_3 and Bi_2Te_3/rGO composite materials, as depicted in Fig. 4E. Each EIS plot comprises a semicircular arc and a sloped region in the high-, medium-, and low-frequency domains.[20] The semicircle corresponds to the resistance from solid electrolyte interface (SEI) formation and charge transfer processes between the electrode and the electrolyte.[41,42] The sloped region signifies the Warburg diffusion phenomenon associated with sodium ion migration within the electrode, manifesting as a 45° slope angle.[43] Consistent with CV and charge–discharge analyses, Fig. 4E reveals that the Bi_2Te_3/rGO

composite electrode exhibits a reduced semicircle diameter compared to its pristine counterpart, indicating diminished interfacial impedance. The inset in Fig. 4E illustrates an equivalent circuit model fitted to the experimental data. Notably, solution resistances (R_s) for pristine and composite electrodes are estimated as 5.14 Ω and 0.88 Ω, respectively. Furthermore, the charge transfer resistance for the Bi_2Te_3/rGO composite is ~113.20 Ω, while that for pristine Bi_2Te_3 nanosheets amounts to 283.00 Ω; this unequivocally demonstrates a significant enhancement in conductivity upon the incorporation of a conductive reduced graphene oxide matrix into the original Bi_2Te_3 nanosheets.

In addition, Fig. 4F and H illustrate the galvanostatic intermittent titration technique (GITT) plots of Bi_2Te_3 and Bi_2Te_3/rGO, respectively, to investigate the diffusion coefficient of the Na ion (D_{Na^+}). It can be calculated using eqn (9):[44]

$$D = \frac{4}{\pi\tau} \left(\frac{m_B V_M}{M_B S} \right)^2 \left(\frac{\Delta E_s}{\Delta E_\tau} \right)^2 \quad (9)$$

Throughout the discharge and charge processes, the D_{Na^+} values for Bi_2Te_3/rGO range from 3.9×10^{-12} to 7.38×10^{-10} cm^2 s^{-1}, exhibiting a notable increase compared to the measurements of pure Bi_2Te_3, which vary from 6.84×10^{-16} cm^2 s^{-1} to 1.1×10^{-12} cm^2 s^{-1}. Consequently, the diffusion coefficient (D_{Na^+}) of Bi_2Te_3/rGO exhibits a notable enhancement compared to that of pure Bi_2Te_3. These findings suggest that the two-dimensional structure of Bi_2Te_3/rGO facilitates Na ion diffusion, thereby improving its rate performance.

Ex situ TEM and *ex situ* XPS analyses were performed at different sodiation/desodiation stages to acquire a thorough comprehension of the structure evolution and electrochemical mechanism of sodium ion storage in the Bi_2Te_3/rGO electrode, as illustrated in Fig. 5. Before sodiation under open-circuit voltage, the XPS spectra of Bi 4f exhibited a pair of peaks at 159.1 and 164.6 eV, which corresponded to the Bi^{3+} states of Bi $4f_{7/2}$ and Bi $4f_{5/2}$. Notably, an additional peak emerged in the XPS spectrum of Te 3d at 564.1 eV, indicating oxygen adsorption on the Te 3d orbitals.[45] Furthermore, compared to the initial position, the peak intensities of Bi^{3+} $4f_{7/2}$, Bi^{3+} $4f_{5/2}$, and Te $3d_{5/2}$ were significantly weakened, suggesting the transformation of Bi_2Te_3/rGO into NaBi and Na_2Te, consistent with the results of EDS elemental mapping (Fig. S4†).

Ex situ TEM further demonstrated the morphology evolution of phase transformation during the discharge–charge process with different potential states. At the discharge state (0.01 V), Fig. 5A illustrates that Bi_2Te_3/rGO undergoes a transition from large grains (approximately 50–100 nm) to uni-
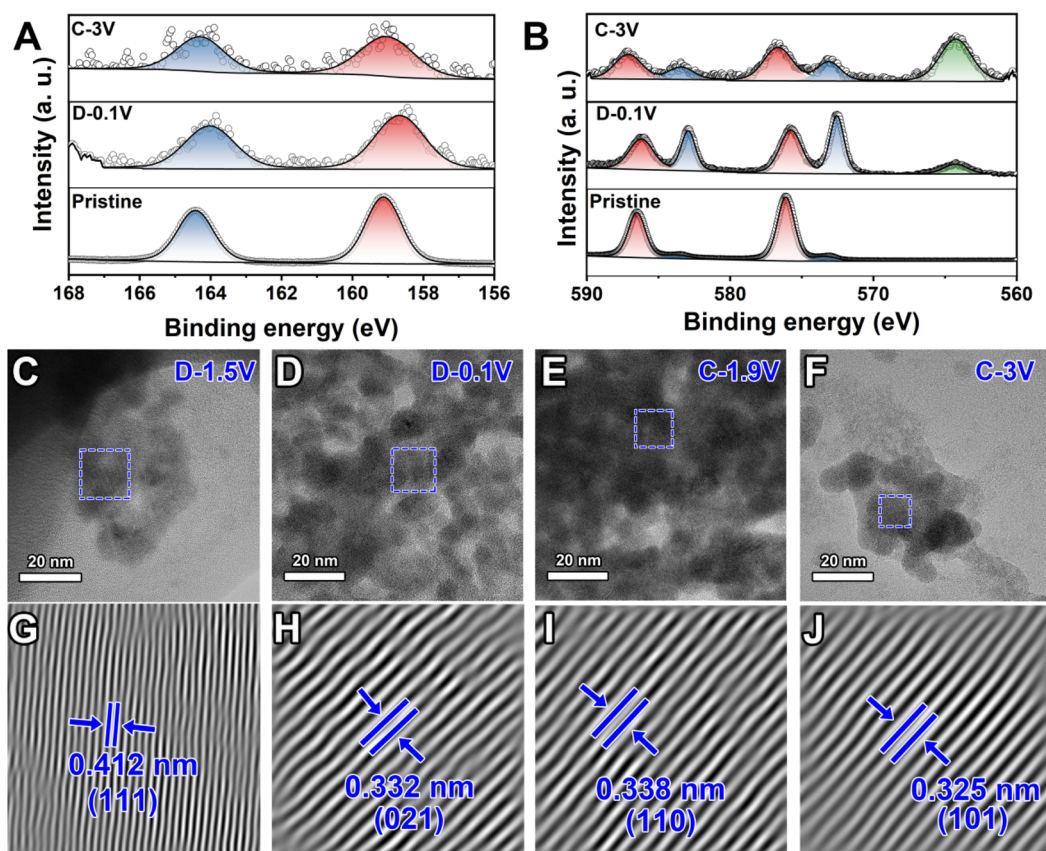
Fig. 5 (A and B) *Ex situ* XPS spectra at various stages during the initial cycle of sodiation/desodiation: (A) Bi 4f and (B) Te 3d. (C–F) HRTEM images and (G–J) initial cycle images of IFFT undergoing sodiation/desodiation: discharged to 1.5 V (C and G) and 0.01 V (D and H); charged to 1.9 V (E and I) and 3.0 V (F and J).

formly dispersed small grains (around 20 nm). In addition, the existence of lattice fringes measuring 0.332 nm apart in Fig. 5H confirms the formation of a Na_3Bi alloy on the (021) plane of Na_3Bi with rhombohedral structure (JCPDS no. 97-067-1309), providing further evidence for *in situ* transformation. The viewpoint is further substantiated by the EDS results (Fig. S3†). Upon being charged back to 1.9 V, the (110) plane of NaBi can be identified from the lattice fringes displayed in Fig. 5I, which have a spacing of 0.338 nm. After charging to 3.0 V, the lattice fringes can be well attributed to Te with a rhombohedral structure (JCPDS no. 97-016-1690) (Fig. 5F and J). Notably, no detectable Bi_2Te_3 lattice is observed after the discharge/charge process, indicating an irreversible transformation within the Bi_2Te_3 nanosheet anode.

Through the utilization of first-principles calculations using density functional theory (DFT), we have comprehensively elucidated the electronic structure and adsorption energy of the Na ion in the material. Furthermore, we investigated the adsorption capability of the material framework for the Na ion and the calculation model in Fig. S5,† where a 2 × 2 × 1 supercell was constructed to accommodate the adsorption of one Na ion. As depicted in Fig. 6A, the Bi_2Te_3/rGO interface shows an adsorption energy of the Na ion measuring −2.37 eV, which is comparatively lower than that observed for Bi_2Te_3

(−2.17 eV). This suggests a pronounced affinity of the Bi_2Te_3/rGO electrode towards the Na ion, thereby facilitating their adsorption and promoting subsequent electrochemical reactions. Insights into the bonding characteristics of the adsorbed Na atoms were obtained by analyzing the difference in electronic density, which involved subtracting the charge density contributions from Na atoms and bare Bi_2Te_3 within the combined compound. As illustrated in Fig. 6B, yellow and cyan electron clouds represent electron accumulation and depletion regions within the Bi_2Te_3/rGO structure. Notably, an evident charge accumulation region around the C atom and an adjacent layer exhibiting electron depletion near the −OH functional group, signifying electron transfer from rGO to Bi_2Te_3, which enhances the Na ion adsorption capacity. In addition, the total densities of states (DOSs) of all samples are illustrated in Fig. 6C and D. It can be observed that Bi_2Te_3/rGO exhibits a conductor behaviour near the Fermi energy level, lacking a band gap, which is considerably superior to Bi_2Te_3, indicating a significant improvement in electronic conductivity due to the rGO confinement effect. Consequently, it can be inferred that preferential adsorption sites for Na ions are more likely to appear around Bi_2Te_3/rGO rather than on pure Bi_2Te_3.

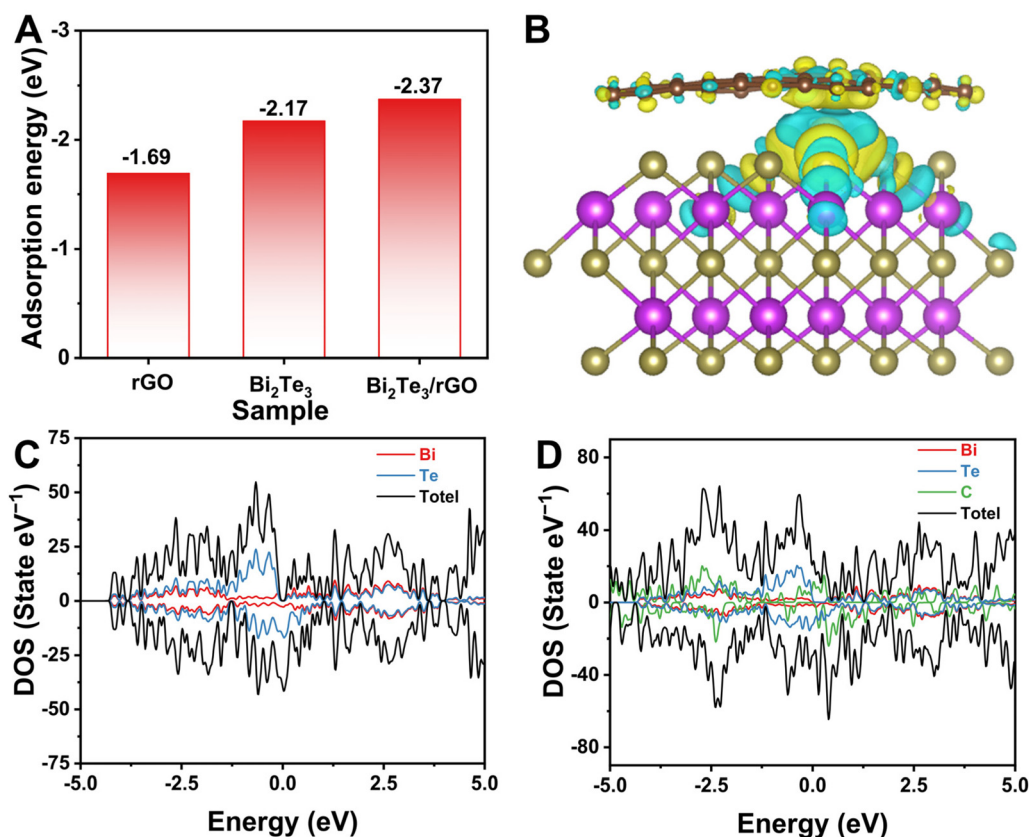The integration of the Bi_2Te_3/rGO anode into a full cell is possible due to its high capacity and outstanding electro-

Fig. 6 (A) Calculated adsorption energies of Na adsorption on the surfaces of rGO, pristine Bi_2Te_3, and Bi_2Te_3/rGO. (B) Differences in the charge density of Na adsorption in the interlayer of the Bi_2Te_3/rGO composite. (C and D) DOSs of Bi_2Te_3 and Bi_2Te_3/rGO composites.

chemical performance, and its evaluation for practical use in SIBs was conducted. We examined the efficiency of the Bi_2Te_3/rGO full cell by utilizing $Na_3V_2(PO_4)_3$ as a cathode. Fig. S6A† illustrates the operational mechanism of the Bi_2Te_3/rGO‖$Na_3V_2(PO_4)_3$ full cell. Na^+ was extracted from the $Na_3V_2(PO_4)_3$ cathode during the charging process and transferred to the Bi_2Te_3/rGO anode. During discharging, Na^+ escapes from the Bi_2Te_3/rGO anode and returns to the $Na_3V_2(PO_4)_3$ cathode again. Fig. S6B† illustrates the exceptional cycling stability of the Bi_2Te_3/rGO‖$Na_3V_2(PO_4)_3$ full cell, which maintains a capacity of 108 mA h g^{-1} and retains 71% of its capacity after 200 cycles. Moreover, the rate performance of the full cell was evaluated at various current densities (Fig. S6C, ESI†), resulting in discharge capacities of 177, 166, 153, 138, 112, and 100 mA h g^{-1} at current densities of 0.1, 0.2, 0.5, 1, 2.0, and 5.0 A g^{-1}, correspondingly. Remarkably, upon returning the current density to its original 0.1 A g^{-1}, the reversible capacity rebounded to 160 mA h g^{-1}, indicating outstanding high-rate performance for sodium storage and potential applications in energy devices. Furthermore, the charge–discharge curves at various current densities exhibit weak polarization even at a high current density of 1 A g^{-1} (Fig. S6D, ESI†), confirming its excellent rate capability.

3. Conclusions

In summary, a universal space-containment strategy was developed to synthesize ultra-small Bi_2Te_3 nanocrystals on rGO. The procedure entails a viable mechanism by accurately adjusting the stacking characteristics of graphene oxide and the pH level of its aqueous dispersion. A slight stacking of graphene oxide sheets can confine the growth of nanocrystals of Bi_2Te_3 in the interlayer nanospaces. As a result of the thermal reduction of graphene oxide to rGO, the Bi_2Te_3/rGO composite material shows a significant capacity for storing Na^+. Boasting an impressive reversible capacity of 521 mA h g^{-1} at 0.1 A g^{-1}, a remarkable rate capacity of 340 mA h g^{-1} at 5 A g^{-1}, and outstanding cycling stability, it retains 82% of its capacity after 800 cycles. The excellent electrochemical performance is a result of the flexible configuration of the nanoplate structure in two dimensions, which guarantees remarkable structural stability and promotes the swift transfer of sodium ions and electrons. *Ex situ* TEM and *ex situ* XPS analyses provide insights into the theoretical basis for the Na^+ storage mechanism in Bi_2Te_3/rGO. Furthermore, the Na ion full cell exhibits good electrochemical performance, combining the Bi_2Te_3/rGO anode with the $Na_3V_2(PO_4)_3$ cathode. This study introduces an innovative approach for constructing two-dimensional Bi_2Te_3/rGO anode materials.

Conflicts of interest

The authors declare no conflict of interest.

Acknowledgements

References

1 G. Dong, L. Li, K. Zhu, J. Yan, G. Wang and D. Cao, *Small*, 2023, 2208291.

2 M. Di, Z. Song, S. Chen and Y. Bai, *Nanoscale*, 2023, **15**, 19159–19167.

3 R. Hu, Y. Tong, J. Yin, J. Wu, J. Zhao, D. Cao, G. Wang and K. Zhu, *Nanoscale Horizons*, 2024, **9**, 305–316.

4 K. Sada, J. Darga and A. Manthiram, *Adv. Energy Mater.*, 2023, **13**, 2302321.

5 J. Chen, G. Adit, L. Li, Y. Zhang, D. H. C. Chua and P. S. Lee, *Energy Environ. Sci.*, 2023, **6**, e12633.

6 X. Song, X. Li, H. Shan, J. Wang, W. Li, K. Xu, K. Zhang, H. M. K. Sari, L. Lei, W. Xiao, J. Qin, C. Xie and X. Sun, *Adv. Funct. Mater.*, 2023, 2303211.

7 N. LeGe, X.-X. He, Y.-X. Wang, Y. Lei, Y.-X. Yang, J.-T. Xu, M. Liu, X. Wu, W.-H. Lai and S.-L. Chou, *Energy Environ. Sci.*, 2023, **16**, 5688–5720.

8 X. Sun, X. Gao, Z. Li, X. Zhang, X. Zhai, Q. Zhang, L. Li, N. Gao, G. He and H. Li, *Small Methods*, 2023, 2300746.

9 S. Chong, L. Yuan, S. Qiao, M. Ma, T. Li, X. L. Huang, Q. Zhou, Y. Wang and W. Huang, *Sci. China Mater.*, 2023, **66**, 2641–2651.

10 S. Chong, J. Yang, L. Sun, S. Guo, Y. Liu and H. K. Liu, *ACS Nano*, 2020, **14**, 9807–9818.

11 R. Meija, V. Lazarenko, Y. Rublova, A. Kons, V. Voikiva, J. Andzane, O. Gogotsi, I. Baginskiy, V. Zahorodna, A. Sarakovskis, A. Pludons, A. Sutka, A. Viksna and D. Erts, *Sustainable Mater. Technol.*, 2023, **38**, e00768.

12 J. H. Moon, H. Seong, G. Kim, Y. Jin, W. Nam, H. Yoo, T. Jung, K. Lee, M. Yang, S. Y. Cho and J. Choi, *Appl. Surf. Sci.*, 2023, **638**, 157976.

13 Z. Li, M. Han, P. Yu and J. Yu, *Adv. Sci.*, 2023, 2306992.

14 X. Xie, X. Wang, Q. Cai, H. Xie and L. Chen, *J. Energy Storage*, 2024, **76**, 109814.

15 R. Tian, H. Zhang, Z. Yuan, Y. Man, J. Sun, J. Bao, M.-S. Wang and X. Zhou, *J. Energy Chem.*, 2024, **89**, 250–258.

16 X. Sun, B. Zhang, M. Chen, L. Wang, D. Wang, R. Man, S. Iqbal, F. Tian, Y. Qian and L. Xu, *Nano Today*, 2022, **43**, 101408.

17 D. Li, J. Hu, C. Wang, L. Guo and J. Zhou, *J. Power Sources*, 2023, **555**, 232387.

18 H. T. Zhang, X. G. Luo, C. H. Wang, Y. M. Xiong, S. Y. Li and X. H. Chen, *J. Cryst. Growth*, 2004, **265**, 558–562.

19 Y. Zhu, J. Zhao, L. Li, J. Xu, X. Zhao, Y. Mi and J. Jin, *Dalton Trans.*, 2021, **50**, 10758–10764.

20 W. Xin, N. Chen, Z. Wei, C. Wang, G. Chen and F. Du, *Chem. – Eur. J.*, 2021, **27**, 3745–3752.

21 Z. Dang, W. Meng, D. Zuo, D. Li, L. Jiang and D. Fang, *Electrochim. Acta*, 2022, **425**, 140752.

22 H. Yin, D. Han, X. Yu, M. Cao, Z. Hou, C. Li and M.-Q. Zhu, *ACS Appl. Energy Mater.*, 2023, **6**, 1155–1175.

23 S. Chong, L. Yuan, Q. Zhou, Y. Wang, S. Qiao, T. Li, M. Ma, B. Yuan and Z. Liu, *Small*, 2023, **19**, 2303985.

24 S. Pang, Z. Hu, C. Fan, W. Zhang, Y. Cai, S. Han, J. Liu and J. Liu, *Nanoscale*, 2022, **14**, 1755–1766.

25 J. Cao, J. Zhong, H. Xu, S. Li, H. Deng, T. Wang, L. Fan, X. Wang, L. Wang, J. Zhu, B. Lu and X. Duan, *Nano Res.*, 2022, **15**, 2040–2046.

26 Q. Peng, S. Zhang, H. Yang, B. Sheng, R. Xu, Q. Wang and Y. Yu, *ACS Nano*, 2020, **14**, 6024–6033.

27 Y. Sun, Q. Wu, K. Zhang, Y. Liu, X. Liang and H. Xiang, *Chem. Commun.*, 2022, **58**, 7120–7123.

28 H. Gu, M. Gao, K. Shen, T. Zhang, J. Zhang, X. Zheng, X. Guo, Y. Liu, F. Cao, H. Gu, Q. Kong and S. Xiong, *Chin. Chem. Lett.*, 2023, 109273, DOI: 10.1016/j.cclet.2023.109273.

29 S. Chong, S. Qiao, L. Yuan, Q. Zhou, T. Li, S. Dong, Y. Wang, M. Ma and W. Huang, *Chem. Eng. J.*, 2023, **461**, 141957.

30 X. Zhou, A. Wang, X. Zheng, Z. Zhang, J. Song, H. Deng, P. Yan, D. Sun, Y. Yang and Z. Lei, *Appl. Surf. Sci.*, 2024, **648**, 159077.

31 J. Xu, J. Jiang, H. Tang, Z. Chen, J. Chen, Y. Zhang and C.-S. Lee, *Adv. Powder Mater.*, 2023, 100169, DOI: 10.1016/j.apmate.2023.100169.

32 C. Guo, S. Yi, R. Si, Y. Wang, H. Liu, F. Yu and J. Li, *Chem. Eng. J.*, 2023, **469**, 143845.

33 M. Qian, Z. Xu, Z. Wang, B. Wei, H. Wang, S. Hu, L.-M. Liu and L. Guo, *Adv. Mater.*, 2020, **32**, 2004835.

34 J. Guo, J. Yang, J. Guan, X. Chen, Y. Zhu, H. Fu, Q. Liu, B. Wei and H. Geng, *Chem. Eng. J.*, 2022, **450**, 138007.

35 D. Li, J. Zhou, X. Chen and H. Song, *ACS Appl. Mater. Interfaces*, 2018, **10**, 30379–30387.

36 M. A. Al-Tahan, B. Miao, S. Xu, Y. Cao, M. Hou, M. R. Shatat, M. Asad, Y. Luo, A. E. Shrshr and J. Zhang, *J. Colloid Interface Sci.*, 2024, **654**, 753–763.

37 Y. Huang, C. Zhu, S. Zhang, X. Hu, K. Zhang, W. Zhou, S. Guo, F. Xu and H. Zeng, *Nano Lett.*, 2019, **19**, 1118–1123.

38 X. Liu, Y. Si, K. Li, Y. Xu, Z. Zhao, C. Li, Y. Fu and D. Li, *Energy Storage Mater.*, 2021, **41**, 255–263.

39 Y.-L. Hou, J.-Z. Chen, B.-H. Zhang, H.-Y. Wang, W.-X. Wen and D.-L. Zhao, *Chem. Eng. J.*, 2024, **479**, 147914.

40 Y. Xi, X. Wang, H. Wang, M. Wang, G. Wang, J. Peng, N. Hou, X. Huang, Y. Cao, Z. Yang, D. Liu, X. Pu, G. Cao, R. Duan, W. Li, J. Wang, K. Zhang, K. Xu, J. Zhang and X. Li, *Adv. Funct. Mater.*, 2023, 2309701.

41 G. Hao, C. Zhang, Z. Chen and Y. Xu, *Adv. Funct. Mater.*, 2022, **32**, 2201352.

42 Z. Zheng, P. Li, J. Huang, H. Liu, Y. Zao, Z. Hu, L. Zhang, H. Chen, M. S. Wang, D. L. Peng and Q. Zhang, *J. Energy Chem.*, 2020, **41**, 126–134.

43 L. Zhong, H. Chen, Y. Sheng, Y. Sun, Y. Xiao, B. Cheng and S. Lei, *J. Energy Chem.*, 2023, **90**, 294–304.

44 Z. Shen, L. Cao, C. D. Rahn, C. Y. Wang and C. Y. Wang, *J. Electrochem. Soc.*, 2013, **160**, A1842–A1846.

45 Z. Zou, Z. Yu, C. Chen, Q. Wang, K. Zhu, K. Ye, G. Wang, D. Cao and J. Yan, *ACS Nano*, 2023, **17**, 13769–13783.